

## Electrical signaling in three-dimensional bacterial biofilms using an agent-based fire-diffuse-fire model

Victor Carneiro da Cunha Martorelli  and Emmanuel Akabuogu 

*Biological Physics, Department of Physics and Astronomy, University of Manchester, Oxford Rd., Manchester M13 9PL, United Kingdom and Division of Infection, Lydia Becker Institute of Immunology and Inflammation, School of Biological Sciences, University of Manchester, Oxford Rd., Manchester M13 9PT, United Kingdom*

Rok Krašovec

*Division of Evolution, Infection and Genomics, School of Biological Sciences, Faculty of Biology, Medicine and Health University of Manchester, Manchester M13 9PT, United Kingdom*

Ian S. Roberts \*

*Division of Infection, Lydia Becker Institute of Immunology and Inflammation, School of Biological Sciences, University of Manchester, Oxford Rd., Manchester M13 9PT, United Kingdom*

Thomas A. Waigh †

*Biological Physics, Department of Physics and Astronomy, University of Manchester, Oxford Rd., Manchester, M13 9PL, United Kingdom and Photon Science Institute, Alan Turing Building, Oxford Rd., Manchester M13 9PY, United Kingdom*



(Received 17 November 2023; accepted 28 March 2024; published 3 May 2024)

Agent-based models were used to describe electrical signaling in bacterial biofilms in three dimensions. Specifically, wavefronts of potassium ions in *Escherichia coli* biofilms subjected to stress from blue light were modeled from experimental data. Electrical signaling occurs only when the biofilms grow beyond a threshold size, which we have shown to vary with the  $K^+$  ion diffusivity, and the  $K^+$  ion threshold concentration, which triggered firing in the *fire-diffuse-fire model*. The transport of the propagating wavefronts shows superdiffusive scaling on time.  $K^+$  ion diffusivity is the main factor that affects the wavefront velocity. The  $K^+$  ion diffusivity and the firing threshold also affect the anomalous exponent for the propagation of the wavefront determining whether the wavefront is subdiffusive or superdiffusive. The geometry of the biofilm and its relation to the mean-square displacement (MSD) of the wavefront as a function of time was investigated for spherical, cylindrical, cubical, and mushroom-like structures. The MSD varied significantly with geometry; an additional regime to the kinetics occurred when the potassium wavefront leaves the biofilm. Adding cylindrical defects to the biofilm, which are known to occur in *E. coli* biofilms, also gave an extra kinetic regime to the wavefront MSD for the propagation through the defect.

DOI: [10.1103/PhysRevE.109.054402](https://doi.org/10.1103/PhysRevE.109.054402)

### I. INTRODUCTION

Bacteria are the most common form of life on planet Earth. There are estimated to be  $10^{30}$  bacteria on our planet that are divided among  $10^{12}$  different species [1,2]. Most bacteria spend most of their time adsorbed to surfaces in communities called biofilms, since there are many advantages for this strategy [3]. Bacterial biofilms consist of a coat of extracellular polymeric substances (EPS) that forms around the communities of bacteria. Bacteria will communicate

among themselves before the formation of a biofilm, and the process is called *quorum sensing*; e.g., they will collectively decide on the suitability of a surface to grow a biofilm by releasing quorum auto-inducer molecules [4]. Bacteria in biofilms are two to three orders of magnitude more resistant to antibiotics than planktonic forms [5]. Thus the study of biofilms and how bacteria communicate to form biofilms can play a critical role in fighting medically relevant infections.

Electrical signaling via small charged ions (e.g.,  $K^+$ ) is a newly discovered phenomenon that occurs in addition to quorum sensing mechanisms and allows bacteria to communicate in small clusters of bacteria and in biofilms [6]. Electrical signaling is possible since the bacteria act as electrically excitable cells (biofilms are an example of excitable matter) similar to neuronal, sensory, and cardiac cells [7,8]. Originally discovered in *Bacillus subtilis* biofilms that experience nutrient starvation [9], similar electrical signaling phenomena have been observed in *Escherichia coli* biofilms due to stress

\*i.s.roberts@manchester.ac.uk

†t.a.waigh@manchester.ac.uk

Published by the American Physical Society under the terms of the [Creative Commons Attribution 4.0 International](https://creativecommons.org/licenses/by/4.0/) license. Further distribution of this work must maintain attribution to the author(s) and the published article's title, journal citation, and DOI.

caused by exposure to blue light (via the creation of reactive oxygen species) [6]. Wave pulses of hyperpolarization have also been observed to propagate through biofilms of *Neisseria gonorrhoeae* [10]. *Pseudomonas aeruginosa* has also been observed to hyperpolarize in response to blue light [11].

The process of electrical signaling in biofilms is an emergent phenomenon due to the interaction of thousands of bacteria and thus lends itself to agent-based modeling (ABM) [12]. Modeling the complex nature of electrical signaling in bacteria is important to understand fundamental aspects of bacterial physiology and to motivate ways to disrupt biofilms; e.g., conducting materials in wound dressings are found to be effective against bacteria [13], but the biophysical mechanisms behind this activity are not well understood.

ABM involves simulations where the agents are constrained to follow a set of rules that determine their interactions, and the rules can be stochastic in nature [14]. ABM can describe complex systems in terms of emergent phenomena from the constituent agents [15]. This is useful to describe bacterial communities as their behavior depends on subtle interactions between the bacteria, e.g., individual bacteria can act like completely different entities at high bacterial concentrations [2]. We previously used ABM to describe electrical signaling in two dimensional *B. subtilis* biofilms [16]. Here we extend the work to three dimensions and use it to describe experiments with the more medically relevant bacterium *E. coli* [6]. A previous study of electrophysiological ABM in three dimensions was used to understand the species independent attraction of bacteria to biofilms [17]. Our study provides a detailed minimal model for electrochemical excitation of biofilms in which nonlinear aspects of the action potentials are neglected. It is found to be sufficient to describe recent fluorescence microscopy experiments from our group with *E. coli* [6], although additional experiments indicate Hodgkin-Huxley modeling of the ion channel dynamics is required to describe electrical impedance spectroscopy experiments and electrical stimulation experiments with fluorescence microscopy. This will be covered in future publications. The current minimal model allows much of the physics to be handled in a simple transparent manner and provides a useful first step for modeling biofilm electrophysiology.

Our simulations allow us to explore the effect of biofilm morphology on the propagation of electrical waves, providing predictions for future experiments. Furthermore, the effect of defects can be studied (cylindrical pores are known to occur in *E. coli* biofilms [18]) and again could motivate future experiments. Finally the anomalous motion of the wavefronts can be studied [19] and the effect of potassium release kinetics quantified. The simulations provide an alternative system to explore the *anomalous transport of wavefronts* in reaction-diffusion systems, which is expected to be a common but rarely explored biophysical phenomenon [20], and the simulations provide an example of emergent anomalous wavefronts from the classical diffusion of ions and the simple linear release kinetics of the ions by the bacteria.

### A. Agent-based models

BSim is an open source Java software package for agent-based modeling [12] that can be used to analyze complex

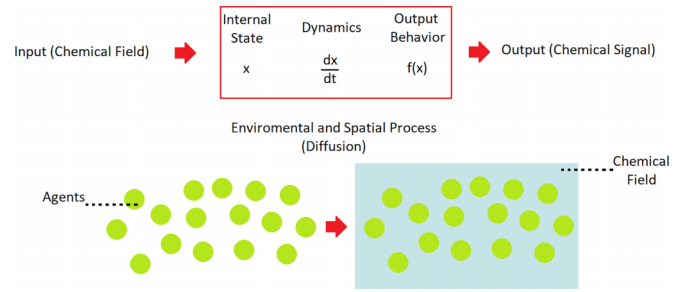


FIG. 1. Schematic of the BSim agent-based model. The two main components of the model are shown: the agents and the process by which agents interact. The agents are shown as green spheres, and the chemical field is shown in blue. BSim allows the partial differential equations for the diffusion of the chemical field to be calculated [21].

behavioral patterns in the dynamics of cell populations [21]. An advantage of BSim is that it is a 3D platform, which makes calculations more realistic compared with previous 2D models of electrical signaling [16,22]. BSim provides an efficient mechanism to describe the release of potassium ions within a community of bacteria, and the internal states of the agents can be carefully controlled.

BSim has two major components to describe electrical signaling in biofilms: the positions of the bacteria (the agents) and the chemical field, which obeys Fick's laws of diffusion (the  $K^+$  ions required for signaling). These main components are shown in Fig. 1, where they can interact in the system through differential equations.

BSim was chosen for the simulation due to its versatility, which allowed the cumulative chemical field (the  $K^+$  ion concentration) from all of the bacterial agents to be calculated. Combined with the user input to determine where the bacteria are located, this allowed any biofilm shape (e.g., a spherical biofilm) to be modeled and the chemical field analyzed as a function of time and space. Numerical solution to Fick's second law of diffusion was used to calculate the transport of  $K^+$  ions for the *fire-diffuse-fire* model.

### B. Fire-diffuse-fire model

A *fire-diffuse-fire* (FDF) model was used by Blee *et al.* to describe electrical signaling in 2D bacterial biofilms [16]. It was originally developed to describe intracellular calcium signaling from discrete sites in eukaryotic cells (*Xenopus oocytes*) to model waves of propagation [7,24–26]. Analytic solutions do not exist for the FDF model for randomly placed sources in two or three dimensions, so agent-based models are needed.

In our FDF model, a spike of potassium was initiated at a specific release site, in an array of stationary bacteria that form the biofilm. When this initial spike propagates via diffusion and reaches a potassium concentration  $c^*$  (the firing threshold) at the position of another bacterium, an additional finite amount ( $\sigma$ ) of potassium ions will be released. This will trigger a chain reaction across the whole biofilm, and the spreading wave of potassium can be numerically analyzed. The system resembles a wildfire in a forest.

The model uses Fick's second law with reaction terms for the release of potassium ions from the bacteria, i.e., it is a variety of reaction-diffusion equation,

$$\frac{\partial c}{\partial t} = D_c \nabla^2 c + \sigma \sum_n \delta(r - r_n) \delta(t - t_n) H(c^* < c), \quad (1)$$

where Fick's second law of diffusion  $\frac{\partial c}{\partial t} = D_c \nabla^2 c$  is used with  $c$  the  $K^+$  ion concentration,  $r$  is the position,  $H$  is the Heaviside function, and  $t$  is the time, coupled with a reaction term for the release of potassium ions from each bacterium. Equation (1) considers a finite number of bacterial agents  $n$  which release an amount  $\sigma$  of  $K^+$  ions into the system at time,  $t_n$ , and at the position of the bacteria,  $r_n$ , when the  $K^+$  concentration is above the firing threshold value  $c^*$ .

The FDF model (1) predicts that the speed of the wavefront is proportional to the diffusion coefficient, which is not observed in experiments [6]. Furthermore, there should be propagation failure of the wavefronts if the diffusion coefficient ( $D_c$ ) is sufficiently small, which is not observed. This is due to the model not allowing the potassium ions to be conserved, which would be more realistic. By adding a constant decay term for the  $K^+$  ions, this problem can be solved,

$$\frac{\partial c}{\partial t} = D_c \nabla^2 c - k_s c + \sigma \sum_n \delta(r - r_n) \delta(t - t_n) H(c^* < c), \quad (2)$$

where  $k_s$  is a constant which allows the ions to be removed from the system, e.g., due to reuptake by the bacteria, and  $H$  is the Heaviside function. This model was studied in two dimensions by Blee *et al.* [16], and data from fluorescence microscopy experiments closely resemble the model with *B. subtilis* biofilms grown in two dimensions. Although the FDF model has its limitations, it is more successful than other standard models, such as *fire and forget* in which the bacteria fire randomly [27]. As the bacteria are acting as a community, the FDF model is more satisfactory in that it can describe the synchronization of the wavefronts [27]. Furthermore, it is possible to motivate the anomalous diffusion of wavefronts via FDF ABM.

### C. Anomalous diffusion of wave fronts

It is interesting to study the dynamics of wavefronts caused by reaction-diffusion phenomena, since it will affect the timing of biological events and the patterns formed [28]. Analytic approaches have predominantly investigated diffusive or ballistic scaling based on analytic solutions to reaction-diffusion equations, but in general anomalous dynamics are possible demonstrating intermediate regimes of behavior. Thus the propagation of wavefronts during electrical signaling in bacteria may not be as straightforward as simple Brownian diffusion, although the  $K^+$  ions are modeled using Fick's second law in Eq. (2). Anomalous diffusion has been observed in experiments with electrochemical wavefronts [9,16] and it is an emergent phenomenon from simulations in two dimensions [16].

The mean-square displacement of the wavefront position ( $R^2$ ) is a useful method to describe how transport occurs

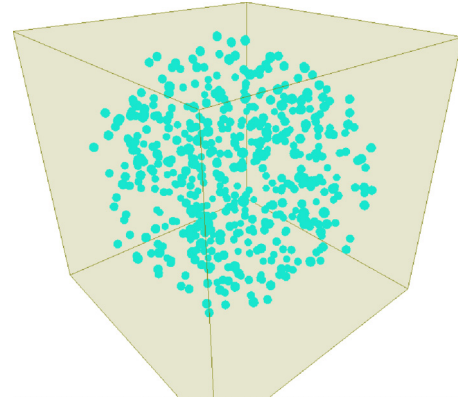


FIG. 2. An example of a spherical biofilm constructed using BSim. The bacteria are stationary and are shown in blue. The EPS is neglected in the model. The bacteria are randomly placed within the sphere, but bacterial overlaps are not permitted. The simulation box is a cube (gray).

in a reaction-diffusion system [29].  $R^2$  is analogous to the mean-square displacement (MSD) of particles used to define the anomalous transport of particles [30],

$$\text{MSD} = D_\alpha t^\alpha, \quad (3)$$

where  $D_\alpha$  is the generalized diffusion coefficient and  $\alpha$  is the scaling exponent. The wavefront of the  $K^+$  ion concentration field can be described using [29]

$$\langle R(t)^2 \rangle = R_c^2 + bt^\gamma, \quad (4)$$

where the MSD  $\langle R(t)^2 \rangle$  of the wavefront position is dependent on a critical radius that will initiate propagation of the wavefront ( $R_c$ ), a constant  $b$ , time  $t$ , and the anomalous scaling constant  $\gamma$ . If  $\gamma = 1$ , the motion of the wavefront is defined to be *diffusive*,  $\gamma < 1$ , the motion is *subdiffusive*,  $1 < \gamma < 2$ , the motion is *subballistic-superdiffusive*, and  $\gamma > 2$ , the motion is *superballistic*. Anomalous transport arises when  $\gamma \neq 0, 1, 2$  [31]. The critical radius ( $R_c$ ) is an emergent phenomenon from the simulations and is required to describe the experiments with *E. coli* [6].

## II. COMPUTATIONAL METHODS

The parameters for the agent-based model include the rate the  $K^+$  ions are removed from the system ( $k_s$ ), the diffusivity of the  $K^+$  ions in the biofilm ( $D_c$ ), the time step, the total simulation time, the bounds of the simulation box, the total amount of  $K^+$  ions, and the threshold concentration for each bacterium to fire ( $c^*$ ). The general parameters used for simulations can be observed in the Supplemental Material [22]. When the threshold concentration is surpassed at the position of a bacterium it will release an additional amount of  $K^+$  ( $\sigma$ ) at its position. There are also time constraints applied for the first peak and second peak of the FDF model, since two propagating wavefronts are observed in *E. coli* experiments in response to light [6], presumably due to the dynamics of a gene network inside each bacterium that handles their response to the reactive oxygen species (ROS) the light creates (a model for adaptation to ROS stress was presented in [6]). The total number of bacteria is also user defined.

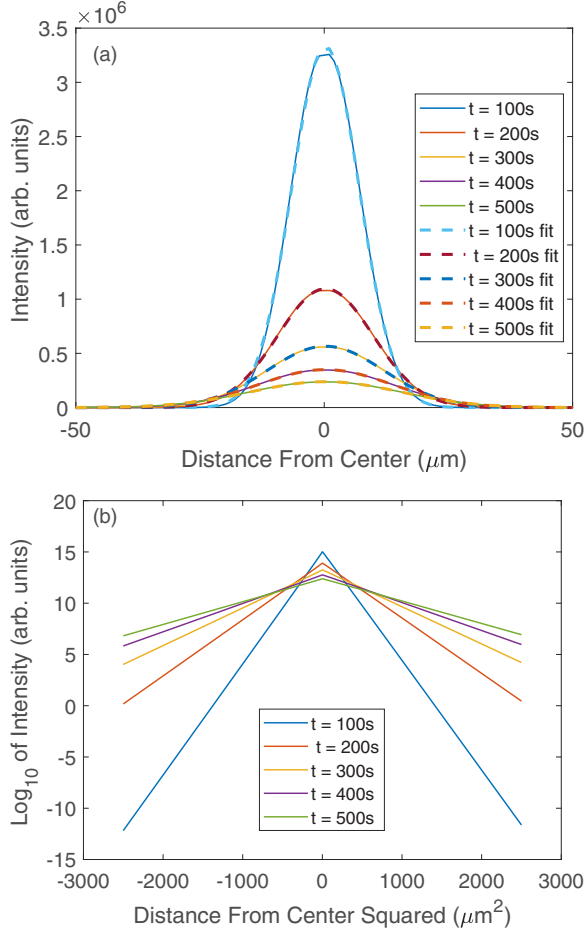


FIG. 3. (a) Simulation of the release of potassium ions of a single bacterium over different time intervals. A single spike occurs in the middle, where the single cell was located as expected from Fick's laws of diffusion, and a decrease in the peak heights occurs over time. A Gaussian curve of the form  $\alpha \exp[-((x - \beta)/\gamma)^2]$  was fit for each of the time curves. For 100, 200, 300, 400, and 500 s the values for  $\alpha$  were  $3.33 \times 10^6$ ,  $1.10 \times 10^6$ ,  $5.66 \times 10^5$ ,  $3.50 \times 10^5$ , and  $2.39 \times 10^5$ , respectively; the values for  $\beta$  were 2.54, 2.54, 2.55, 2.55, and 2.56, respectively; the values for  $\gamma$  were 9.64, 13.6, 16.6, 19.1, and 21.3, respectively. The fits all corresponded to a  $R^2$  value of 0.9999. (b) The logarithm of the intensity and the square of the distance were considered to ensure it is Gaussian. The straight lines suggest that the trend is of Gaussian nature, though it is slightly off-center due to the discrete nature of the lattice, i.e., a one-pixel bias. The potassium diffusivity ( $D_c$ ) was  $0.1 \mu\text{m}^2/\text{s}$  and the decay constant ( $k_s$ ) was set to a value of  $4.44 \times 10^{-4}$ . The quantity of potassium ions added ( $\sigma$ ) was  $5 \times 10^9$ .

A spherical geometry was first used to describe the biofilm (Fig. 2). The bacteria were static i.e., immotile and not dividing on the timescale of the experiment. The bacterial agents were arranged randomly within the workspace by defining two characteristic spherical coordinates  $\theta$  and  $\phi$ ,

$$\begin{aligned} \theta &= 2\pi u, \\ \phi &= \cos^{-1}(2v - 1). \end{aligned} \quad (5)$$

The variables  $u$  and  $v$  were defined as random numbers from 0 to 1. Therefore, random angles for  $\theta$  and  $\phi$  were obtained for

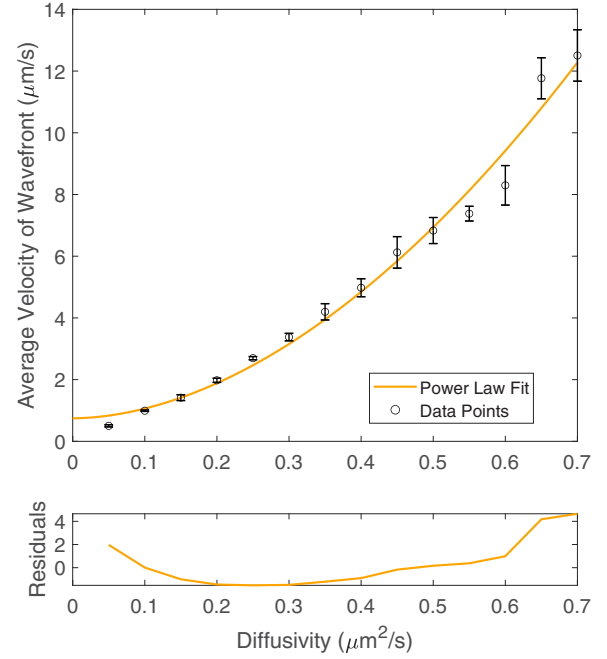


FIG. 4. Average velocity of a wavefront of  $\text{K}^+$  ions as a function of ion diffusivity, averaged over three simulations. The decay rate ( $k_s$ ) was kept constant at  $4.44 \times 10^{-4}$  molecules per second and the  $\text{K}^+$  ions released was kept constant at  $5 \times 10^9$  molecules in the FDF model for the whole biofilm. The firing threshold ( $c^*$ ) was maintained at  $7 \times 10^6$ . The method for determining the intensities was the spherical shell method. The error bars show the standard error on the mean of three runs. The power-law fit was of the form  $f(x) = ax^b + c$ , where  $a = 22.3$ ,  $b = 1.85$ , and  $c = 0.75$ . It had a regression  $\Lambda^2$  value of 0.9831.

the spherical coordinates. The random angles were assigned to their respective Cartesian coordinates  $x_0$ ,  $y_0$  and  $z_0$  using the transformation,

$$\begin{aligned} x_0 &= \sin(\phi) \cos(\theta), \\ y_0 &= \sin(\phi) \sin(\theta), \\ z_0 &= \cos(\phi). \end{aligned} \quad (6)$$

This takes a random point from 0 to 1 for each coordinate that will fall inside a unit sphere. The points in the workspace of the sphere ( $x_{00}$ ,  $y_{00}$ ,  $z_{00}$ ) are then assigned,

$$\begin{aligned} x_{00} &= \frac{1}{2} R x_0 x_b, \\ y_{00} &= \frac{1}{2} R y_0 y_b, \\ z_{00} &= \frac{1}{2} R z_0 z_b, \end{aligned} \quad (7)$$

where  $R$  is the cube root of a random variable from 0 to 1, which will help ensure a spherical symmetry within the workspace.  $x_b$ ,  $y_b$ , and  $z_b$  are the boundary extents of the workspace. A sphere is created with radius half the size of the workspace. An extra restriction ensures the bacteria do not overlap by assigning an "if" statement to delete attempts to place bacteria within  $r$  (the size of a bacterium) of the same location. Figure 2 shows a spherical biofilm generated with 6000 bacteria. Both reflecting and periodic boundary

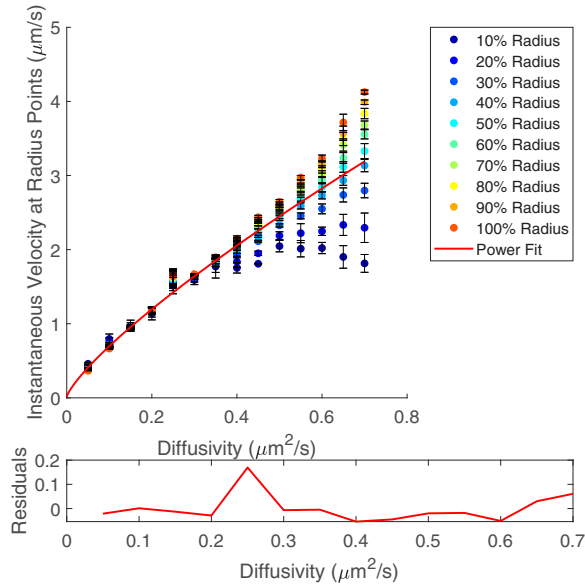


FIG. 5. The instantaneous velocity of  $K^+$  ion wavefronts as a function of  $K^+$  diffusivity calculated for a range of radii. An average of three simulations is shown. The decay rate ( $k_c$ ) was kept constant at  $4.44 \times 10^{-4}$  molecules per second, and the amount of potassium ions released ( $\sigma$ ) was kept constant at  $5 \times 10^9$  molecules in the FDF model. The firing threshold ( $c^*$ ) was maintained at  $7 \times 10^6$ . The error bars are the standard error on the mean of three simulations. The power-law fit of the average for each diffusivity point was of the form  $v(D) = aD^b + c$ , where  $a = 4.21$ ,  $b = 0.79$ , and  $c = 0.014$ . It had a regression  $\Lambda^2$  value of 0.9958.

conditions can be implemented for calculations of the chemical field (the  $K^+$  ion concentration).

In all the biofilm geometries explored, the bacteria are initially spiked only once and there can be more than one bacteria in the volume of the initial spike. The result of the

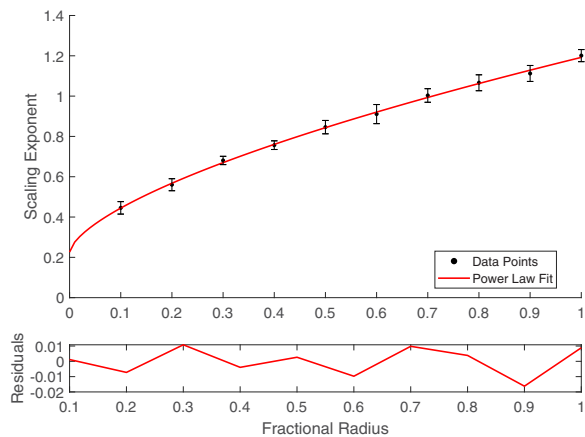


FIG. 6. Power-law scaling exponents of the instantaneous velocity of the  $K^+$  ion wavefront as a function of radial position inside the biofilm for an average of three runs (the fractional radius = 1 on the edge of the biofilm). The decay rate ( $k_c$ ) was kept constant at  $4.44 \times 10^{-4}$  molecules per second, and the ions released ( $\sigma$ ) were kept constant at  $5 \times 10^9$  in the FDF model. The error bars are the standard error mean of the three runs. The power law was in the form of  $f(R) = aR^b + c$ , where  $a = 0.97$ ,  $b = 0.65$ , and  $c = 0.23$ . It had a regression  $\Lambda^2$  value of 0.9987.

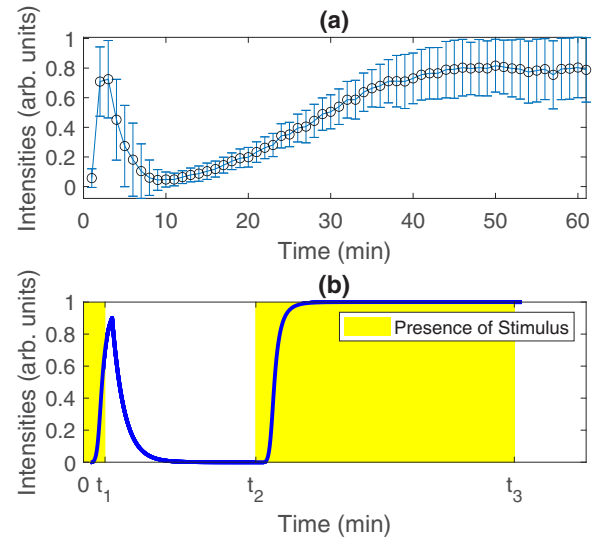


FIG. 7. Globally averaged fluorescence intensity from (a) experimental data compared to (b) simulation data. (a) ThT was used as a Nernstian probe in fluorescence microscopy experiments with an *E. coli* biofilm [6]. The error bars in the top subfigure represent the standard deviation over more than three experiments. (b) The global oscillations for the bottom figure are taken for a simulation with  $K^+$  diffusivity ( $D_c$ ) of  $0.1 \mu\text{m}^2$ , decay rate ( $k_c$ ) of  $5 \times 10^{-3}$  molecules/s,  $5 \times 10^9$  potassium ions ( $\sigma$ ) added per spike, and  $1 \times 10^7$  potassium ions as the firing threshold ( $c^*$ ) for the FDF mechanism. The first wavefront of the FDF stops at  $t_1 = 180$  sec and the second wavefront begins (a new spike) at  $t_2 = 1440$  sec. The simulation stops at  $t_3 = 3600$  sec.

initial stimulation is thus dependent on the number of bacteria. Propagation failure can occur if no bacteria are found in the region of initial spiking. However, this is unlikely due to the total number of bacteria used and was not observed in the current simulations.

After the initial stimulation, the wavefront began to propagate through the biofilm. If the time of the stimulation is shorter than an initial wavefront parameter (in seconds), which is defined as the time over which the wavefront will stop propagating, the FDF mechanism continues. If the stimulation time is lower than a second wavefront parameter (in seconds), which is defined as the time at which the wavefront will begin propagating again (the second wavefront), but higher than the initial wavefront parameter, then the loss mechanism dominates, i.e., the fire-diffuse-fire mechanism stops and the wavefront stops propagating. Finally, if the stimulation time is higher than the second wavefront time parameter, it will continuously propagate the FDF mechanism. After all of the conditions and statements are completed, each time step is finished and the chemical field gets updated. One can toggle between showing the bacteria and the chemical field (the  $K^+$  concentration).

### Measuring wavefront velocity

The wavefront position was defined using the threshold concentration ( $c^*$ ) of the potassium ions for propagation. The code has a loop that checks the ion concentrations first in time and then in space. When the potassium ion concentration is higher than the threshold ( $c^*$ ), a value of one is assigned

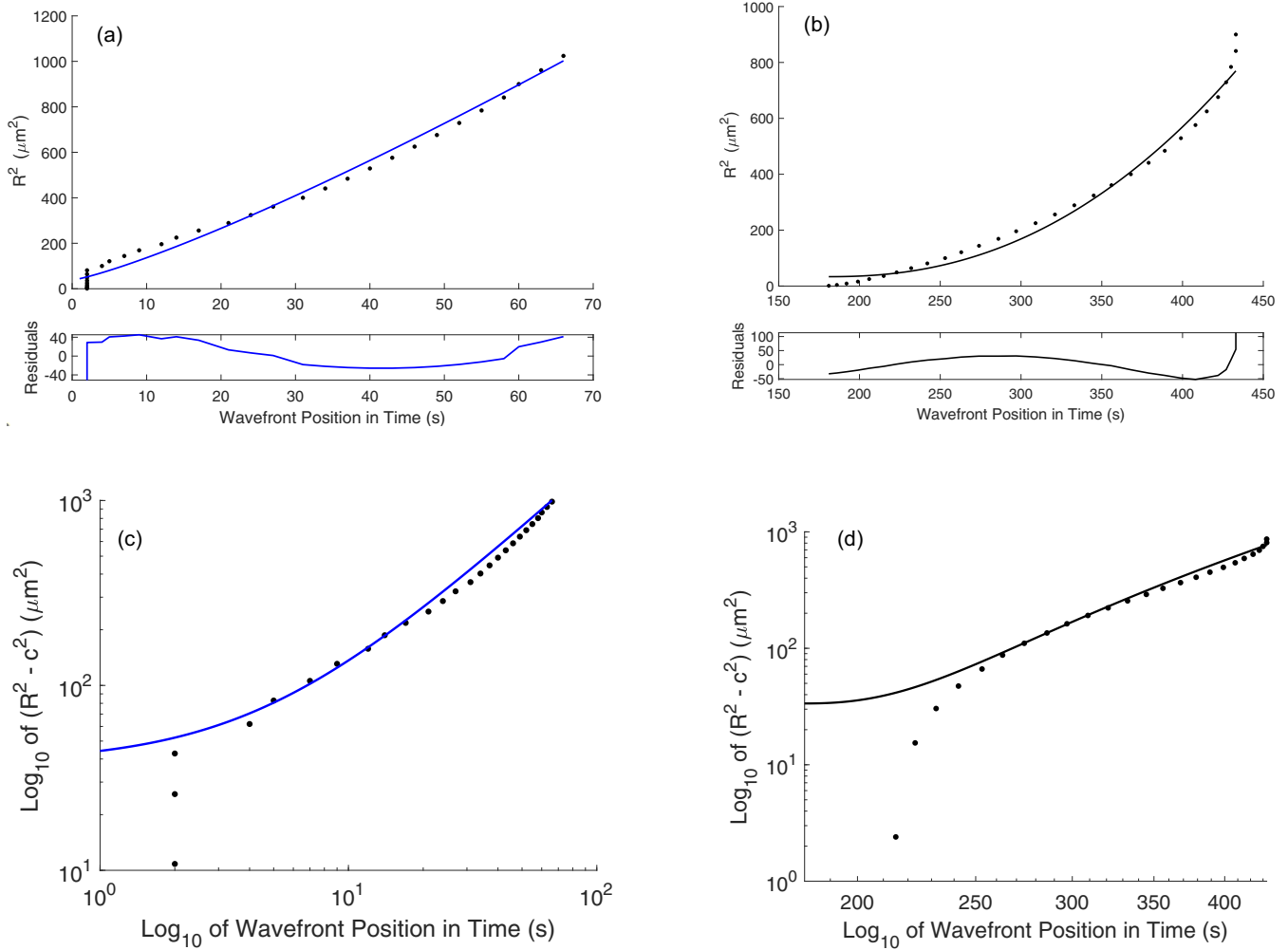


FIG. 8. Mean-square displacement of (a) centrifugal and (b) centripetal  $K^+$  wavefronts for a simulation with  $K^+$  diffusivity of  $0.1 \mu\text{m}^2$ , decay rate ( $k_e$ ) of  $5 \times 10^{-3}$  molecules/s,  $5 \times 10^9$  quantity of  $K^+$  ( $\sigma$ ) added per hyperpolarization event and  $3 \times 10^9$  molecules as the threshold ( $c^*$ ) for the firing mechanism. (a) The curve fit is Eq. (4), where  $\gamma$  is  $1.21 \pm 0.12$  and  $R_c$  is  $6.17 \pm 1.84 \mu\text{m}$ . The regression  $R^2$  value is 0.9911. The residuals of the model are plotted underneath the main graph. (b) The curve fit is again Eq. (4), where  $\gamma$  is  $2.26 \pm 0.31$  and  $R_c$  is undefined due to the nature of the centripetal wavefront. The regression  $R^2$  value is 0.9840. The residuals of the model are plotted underneath the main graph. (c) Logarithmic plot for the time and  $R^2 - c^2$  for the centrifugal wavefront; (d) logarithmic plot for the time and  $R^2 - c^2$  for the centripetal wavefront.

to that radius, so that the wavefront is known to be at that position. Afterwards, the indices of the ones are all retrieved, which gives the time and space coordinates for the wavefront. If the wavefront is inwards rather than outwards, then simply flipping the array and assigning the wavefront position for values below the threshold provides a useful definition.

Once the position of the wavefront is found, it is straightforward to plot the time against the position and fit a polynomial. The derivative of the curve is a reasonable approximation to the instantaneous velocity of the wavefront at different points in time and space.

### III. RESULTS

#### A. $K^+$ Ion diffusion from a single bacterium

To confirm that the diffusion code functions accurately in Bsim and is consistent with Fick's laws of diffusion, the diffusion profile for release of potassium ions from a single

bacterium was investigated. A single bacterium was placed in the center of the 3D workspace, and it was fired once. The diffusion profile of the  $K^+$  ions at different times was then calculated for a single bacterium as a function of distance.

In Fig. 3 Fick's laws of diffusion appear to be simulated correctly for a single bacterium. The ion concentration follows a Gaussian form with log (base 10) intensity proportional to  $r^2$ . The slight asymmetry in the logarithmic concentration profiles [Fig. 3(a)] is due to the discrete positioning of the bacterium magnified by the logarithmic scale; i.e., a slight asymmetry exists due to a one-pixel offset.

#### B. Average wavefront velocity and $K^+$ ion diffusivity

The average velocity of the centripetal (outward moving) wavefront was calculated at each point along Cartesian axes superposed on the spherical biofilm. A movie of complete simulations is shown in the supplemental videos in which

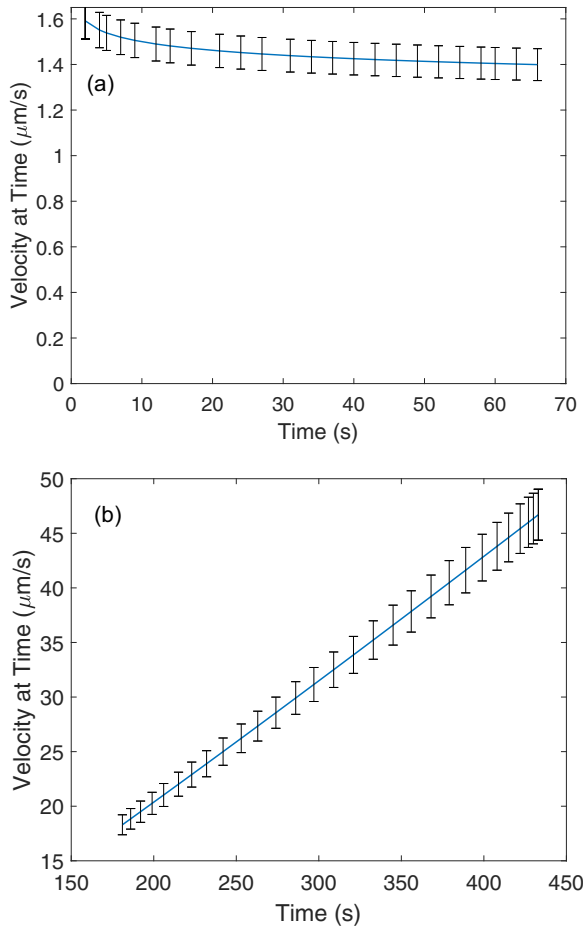


FIG. 9. Instantaneous velocity as a function of time of (a) the centrifugal and (b) centripetal  $\text{K}^+$  wavefronts for simulations where the  $\text{K}^+$  diffusivity ( $D_c$ ) is  $0.1 \mu\text{m}^2$ , the decay rate ( $k_c$ ) is  $5 \times 10^{-3}$  molecules/s, the quantity of  $\text{K}^+$  added per hyperpolarization event ( $\sigma$ ) is  $5 \times 10^9$ , and  $3 \times 10^9$  molecules as the firing threshold ( $c^*$ ) for the FDF mechanism.

the bacterial agents are invisible to allow a better view of the chemical field propagation and an outline of the shape is provided [22]. These agents, however, were present in the calculations.

Figure 4 shows the average velocity of the  $\text{K}^+$  wavefront as a function of the diffusivity of the  $\text{K}^+$  ions. As expected, the average wavefront velocity increases as the  $\text{K}^+$  diffusivity increases.  $\text{K}^+$  ions diffuse at a constant rate in bulk water consistent with the Stokes-Einstein equation [32], but extra cellular polymeric substance in the biofilm can reduce the value of effective diffusion coefficients (more EPS will reduce  $D_c$ ), and thus it is interesting to explore the effects of this parameter. Power-law fits of the average wavefront velocity on  $\text{K}^+$  ion diffusivity gives the scaling exponent  $b = 1.85$ .

### C. Instantaneous velocity and $\text{K}^+$ ion diffusivity

To measure the instantaneous velocity of the  $\text{K}^+$  wavefronts, a polynomial curve was fit to the position of the wavefront as a function of time. Then the time derivative was taken to give the instantaneous velocity.

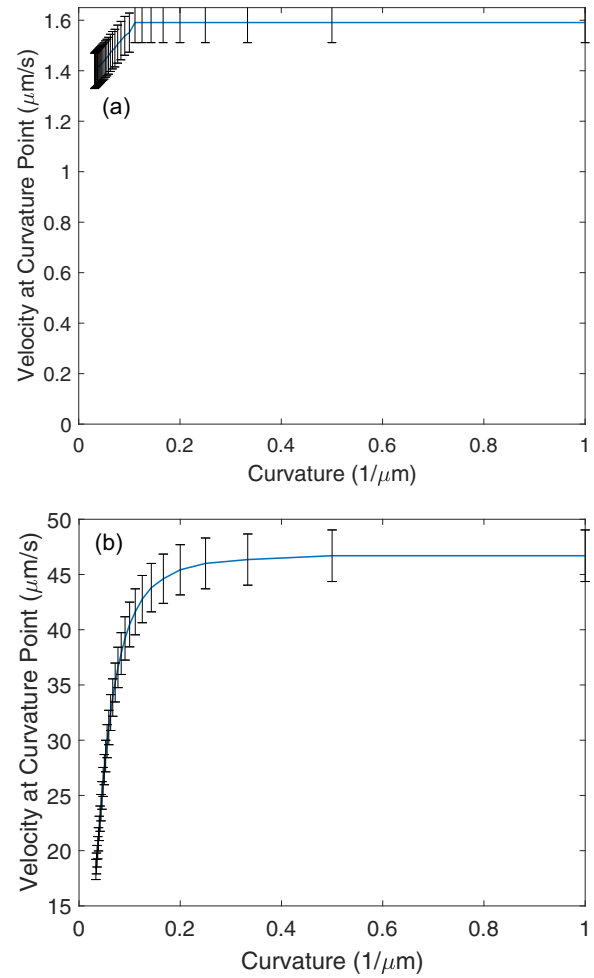


FIG. 10. Instantaneous velocity as a function of curvature ( $= 1/R$ ) for (a) the centrifugal and (b) the centripetal wavefronts from simulations with  $\text{K}^+$  diffusivity ( $D_c$ ) of  $0.1 \mu\text{m}^2$ , decay rate ( $k_s$ ) of  $5 \times 10^{-3}$  molecules/s,  $5 \times 10^9$  quantity of  $\text{K}^+$  ( $\sigma$ ) added per hyperpolarization event, and  $3 \times 10^9$  molecules as the firing threshold ( $c^*$ ) for the FDF mechanism. The radius is defined as zero at the center of the biofilm, and the biofilm periphery is the maximum radius. The error bars show the 95% confidence interval for the velocities.

The instantaneous wavefront velocity calculated at different radii from the point of initial spiking is shown in Fig. 5 as a function of  $\text{K}^+$  ion diffusivity. There is a steady increase of the wavefront velocity with the radius following a power law of the form of  $v(D) = aD^b + c$ , where  $a = 4.21$ ,  $b = 0.79$ , and  $c = 0.014$ . The scaling exponent is significantly lower for the instantaneous velocity than for the average velocity in Fig. 4. Figure 6 shows how the scaling exponent  $b$  for the instantaneous velocity depends on the radius of the biofilm (rescaled to form a fractional radius on the figure).

### D. $\text{K}^+$ ion profile averaged over the entire biofilm

Experimentally, two hyperpolarization events occur in *E. coli* biofilms in response to illumination with blue light, and they can be observed in globally averaged intensity profiles from fluorescence microscopy experiments using ThT as a fluorescent Nernstian probe [6]. The first hyperpolarization event is when the bacteria initially respond to the blue light,

and the second hyperpolarization event is thought to be a habituation phenomenon. These global oscillations could be described by the FDF ABM simulations. This is done by setting two spikes of hyperpolarization which will trigger the FDF model, and these spikes will be triggered at different time intervals which follow the experimental data. The potassium ion concentration is then globally averaged over the entire simulation box. The two hyperpolarization events are shown in Fig. 7. The simulations are in reasonable agreement with experiment.  $t_1$  is the time for the first centripetal wavefront (the first hyperpolarization event),  $t_2$  is the time for the centrifugal wavefront (recovery), and  $t_3$  is the time for the second centripetal event (the second hyperpolarization event). However, the second hyperpolarization event occurs more abruptly with the simulation than with the experiment.

### E. Simulation of the wavefront dynamics

To understand the propagation of ion channel signaling in a 3D biofilm, the  $K^+$  wavefront was analyzed by fitting Eq. (4) to the mean-square displacement of the  $K^+$  wavefront position and the equation provides an empirical definition of the *anomalous wavefront dynamics* [29]. The hyperpolarization and depolarization wavefronts are denoted as the *centripetal* and *centrifugal* wavefronts respectively. The simulations were used to describe the experimental data.

The centrifugal  $K^+$  wavefront has a power-law scaling exponent  $\gamma$  of 1.21 and is thus superdiffusive. This is shown in Fig. 8(a), and the critical radius for propagation of the wavefront was  $6.2 \pm 1.8 \mu\text{m}$ . The centripetal wavefront has a value of  $\gamma$  of 2.26 and is thus superballistic. This is shown in Fig. 8(b). The power-law exponent can be better appreciated in the logarithmic scale plots of both centrifugal and centripetal wavefronts shown in Figs. 8(c) and 8(d).

The  $K^+$  wavefront velocity as a function of time is shown in Fig. 9. The velocity of the centrifugal wavefront was almost constant with time, whereas the centripetal wavefront has a linear increase.

Another characteristic of the  $K^+$  wavefront is how its velocity depends on its radius of curvature. In cardiac tissue (another classic example of excitable matter) a complex interplay between wavefront curvature and velocity is observed, and it is related to cardiac physiology, e.g., pacing of the heart with scroll waves [7]. For a  $K^+$  ion wavefront in a spherical biofilm, the curvature can be approximated by the reciprocal of the radius of the wavefront,  $1/R$ .

Figure 10(a) shows how the instantaneous velocity of the  $K^+$  wavefront changes as a function of its curvature for the centrifugal wavefront. The centrifugal  $K^+$  wavefront has almost no dependence on curvature, whereas the centripetal wavefront, shown in Fig. 10(b) has a monotonic increase which plateaus at high curvatures [7]. Analytically the Eikonal approximation predicts the instantaneous wavefront velocity ( $v$ ) is proportional to the curvature ( $1/R$ ),  $v \propto 1/R$ , in reasonable agreement with the behavior of the centripetal wavefront [7].

### F. Experimental wavefront dynamics

Confocal microscopy was used to measure the  $K^+$  wavefront dynamics in 3D using the fluorescent dye ThT as a

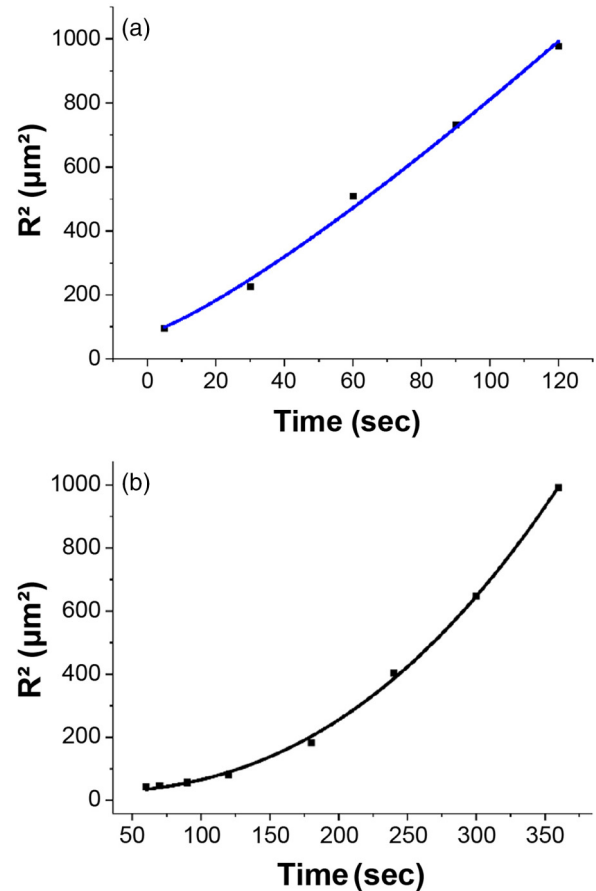


FIG. 11. Mean-square displacement of (a) the centrifugal and (b) centripetal  $K^+$  wavefronts as a function of time measured using confocal microscopy with ThT fluorophores. (a) The curve fit is Eq. (4), where  $\gamma$  is  $1.22 \pm 0.15$  and  $R_c$  is  $4.71 \pm 0.98 \mu\text{m}$ . (b) The curve fit is Eq. (4), where  $\gamma$  is  $2.43 \pm 0.08$  and  $R_c$  is undefined due to the nature of the centripetal wavefront.

Nernstian voltage probe. The confocal microscopy technique allows good resolution along the  $z$  axis (transverse axis) of thick biological samples and allows vertical optical sectioning. The thickness of the biofilm shown in Fig. 8 was  $154 \mu\text{m}$ . The sample was exposed to blue light stimulation for 60 minutes [6]. The intensity profile from confocal microscopy suggests that the biofilm begins to spike at a depth of  $78 \mu\text{m}$ . Multiple optical sections were made at different equally spaced distances from the center of the biofilm, perpendicular to the  $z$  axis of the wavefront. The radial distance was measured from the core to the periphery. Figure 11 shows the mean-square displacement of the wavefront position  $R^2$  as a function of time. The critical radii and the scaling exponents  $\gamma$  are very close to the model predictions. The centrifugal wavefront anomalous exponents were  $1.21 \pm 0.12$  and  $1.22 \pm 0.15$  for the model and experiment, respectively. The critical radius was in reasonable agreement at  $6.2 \pm 1.8 \mu\text{m}$  and  $4.7 \pm 1.0 \mu\text{m}$  for the model and experiment, respectively.

How the velocity varies with time and radius for the experimental confocal microscopy results was also investigated. There is a nonlinear dependence of the wavefront velocity on

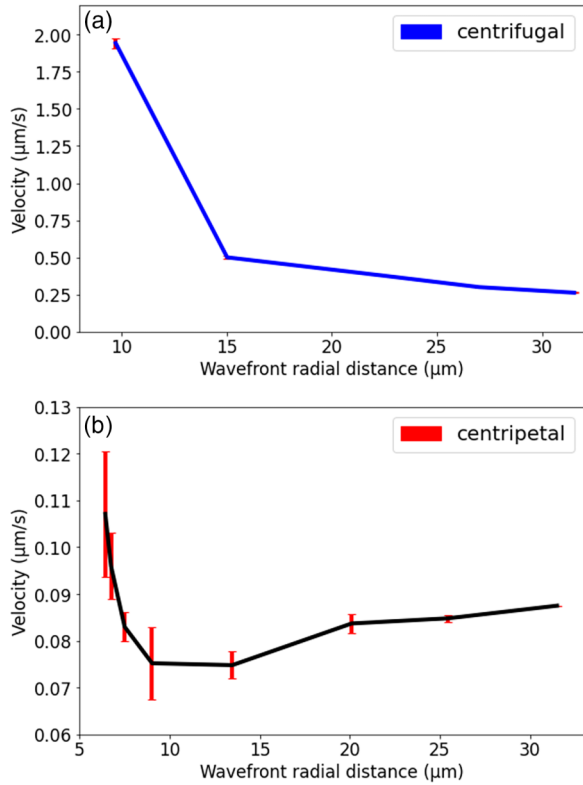


FIG. 12. Instantaneous velocity as a function of radius of (a) the centrifugal and (b) the centripetal K<sup>+</sup> wavefronts measured from the first peak of the confocal microscopy data. An inverse relation of the K<sup>+</sup> wavefront velocity is observed with radius for (a), whereas (b) has a minimum. The error bars are the standard deviation of more than three experiments.

the radius, Fig. 12, and on time, Fig. 13, for both centrifugal and centripetal wavefronts.

### G. Anomalous diffusion of the wavefront

Factors affecting anomalous diffusion of the K<sup>+</sup> wavefronts were explored. In Fig. 14(a) for lower diffusivities of the potassium ions the mean-square displacement position ( $R^2$ ) behaves in a more superballistic manner ( $R^2 > t^2$ ), whereas for higher diffusivities it tends to become more diffusive ( $R^2 \sim t^1$ ). The base 10 log plot shown in Fig. 14(b) shows a clearer picture with the power laws.

Figure 15 shows the mean-square displacement of the K<sup>+</sup> wavefronts as a function of time. The anomalous diffusion also varies with the firing threshold ( $c^*$ ). This suggests that the higher the values of the threshold, the less ballistic is the wavefront i.e., the lower the anomalous scaling exponent ( $\alpha$ ) in Eq. (4).

### H. Critical radius of biofilms for propagating wavefronts

A critical radius for propagation of potassium wavefronts was observed in the simulations, in agreement with experiments. The critical radius is a measure of how much the initial spike needs to move before the wavefront propagates across the whole biofilm. The critical radius was found to be independent of the firing threshold ( $c^*$ ) of the FDF model. The

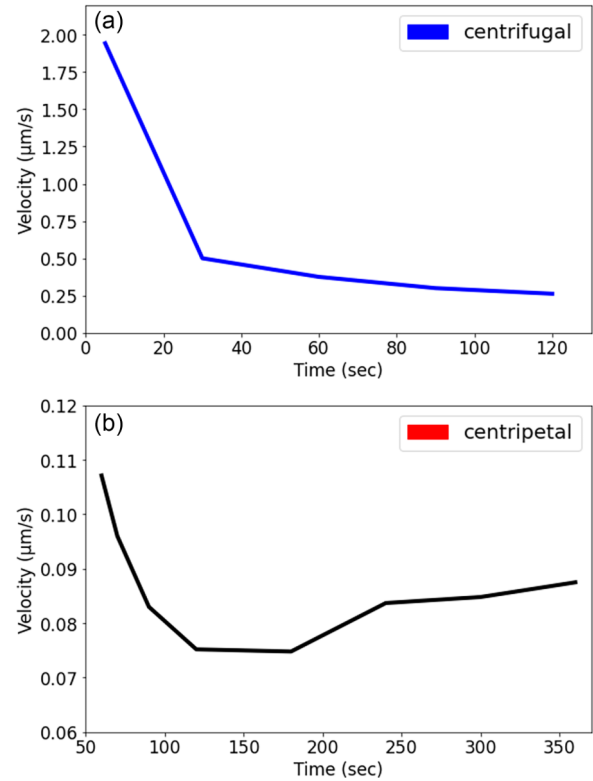


FIG. 13. Instantaneous velocity as a function of time for (a) the centrifugal and (b) the centripetal K<sup>+</sup> wavefronts measured from the first hyperpolarization event of the confocal microscopy data. An inverse relationship of the wavefront velocity with time is shown for (a), whereas (b) has a minimum. The error bars are the standard deviation of more than three experiments.

critical radius decreases nonlinearly with the diffusivity of the potassium ions (Fig. 16) and higher K<sup>+</sup> diffusivity creates smaller critical radii.

The critical radius for K<sup>+</sup> wavefront propagation was not affected by the density of the bacteria in the biofilm in the simulations. For lower bacterial numbers, the wavefront did not propagate. Also the decay rate of potassium ions ( $k_s$ ) does not seem to influence the critical radius.

### I. Different biofilm geometries

Biofilms in nature grow in a variety of shapes and sizes [33] Although the spherical biofilm was useful due to its simplicity, other geometries are also interesting. Furthermore, defect structures in cylindrical biofilms were explored, since they will be common in nature, e.g., foreign particles often occur in biofilms, including foreign nonspiking bacteria, and water-filled cylindrical transport pores are actively maintained by *E. coli* in their biofilms [18].

The different biofilm shapes used for testing the global intensity of the hyperpolarization events (the K<sup>+</sup> concentration) are shown in Fig. 17. These events are noted to be relatively independent of the biofilm shape (Fig. 18).

To understand the dependence of the squared radial displacement of the K<sup>+</sup> wavefronts as a function of time for the different geometries, three parallel axes perpendicular to

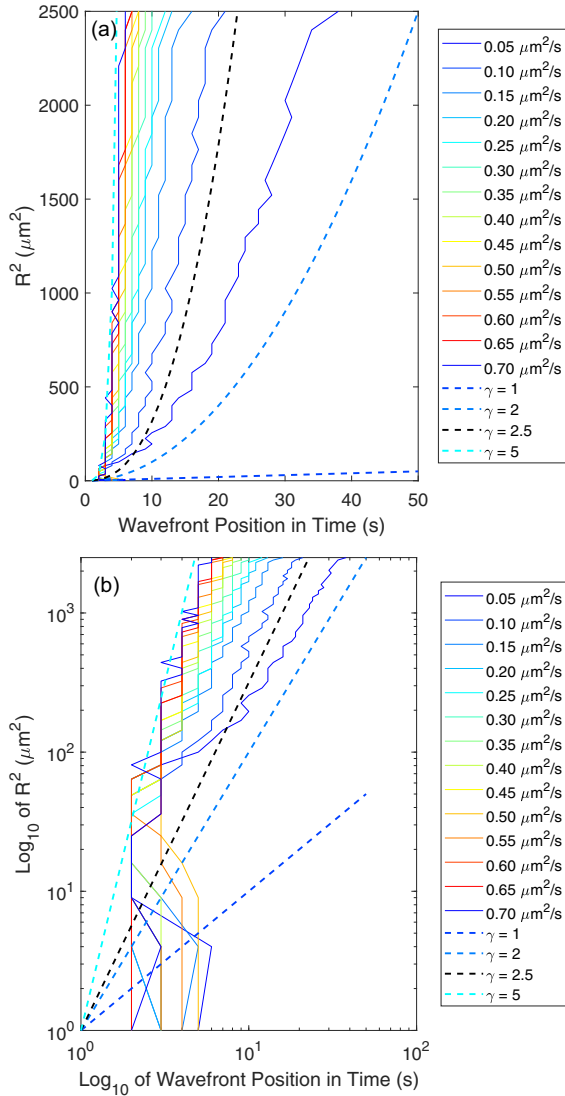


FIG. 14. (a) Mean-square displacement of  $K^+$  wavefronts as a function of time for different  $K^+$  diffusivities from ABM simulations. The different colors represent the different  $K^+$  diffusivities shown in the legend. All  $K^+$  diffusivities are given in  $\mu m^2/s$ . The dashed trendlines for different  $\gamma$  power-law scaling exponents are also shown for reference. (b) The plot in (a) but scaled in a logarithmic manner (base 10).

the y axis were used [Fig. 19(a)] where in axis 1, the initial spike will take place instead of the center for the cylinder with a defect. This allowed the wavefront propagation from three reference points surrounding a defect to be explored. This is shown in Fig. 20 for the different geometries. Different regimes are highlighted with trend-lines for different  $\gamma$  values. Furthermore, making these biofilms small, will also create an additional regime due to the size relative to the overall simulation space. This is shown in Fig. 21 for the smaller geometries.

**J. Release and dormancy times of  $K^+$  ions by bacteria**

The kinetics of  $K^+$  ion release by the bacteria was investigated. Initially the concentration profile used for  $K^+$  release

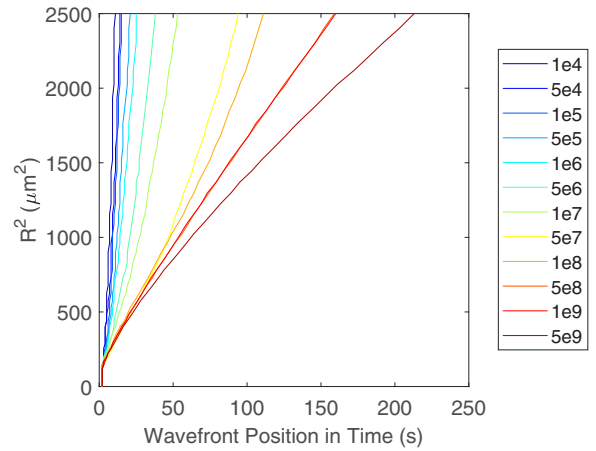


FIG. 15. Mean-square displacement of the  $K^+$  wavefronts as a function of time for different  $K^+$  concentration firing thresholds ( $c^*$ ) from ABM simulations. The different colors represent the different firing thresholds shown in the legend. All firing thresholds are given in terms of the number of molecules needed to trigger the FDF mechanism.

was similar to a delta function, Fig. 22(a). The potassium ions are instantly released once the bacterium is above the threshold concentration ( $c^*$ ) and the width of the pulse is limited by the time step of the simulation. More realistic behavior is provided by adding a rise time for how long the cell will release the chemical and a dormancy time for when the cell will not fire even if it is above the firing threshold (similar to the refractory period of a neuron [7]), Fig. 22(b). These release characteristics were used for a spherical biofilm, and the  $R^2$  and total intensity were measured for different rise and dormancy times.

One, 5, and 10 s were chosen for both the rise and the dormancy times for the cells, and the  $R^2$  of the  $K^+$  wavefront was plotted as a function of time, Fig. 23. A superdiffu-

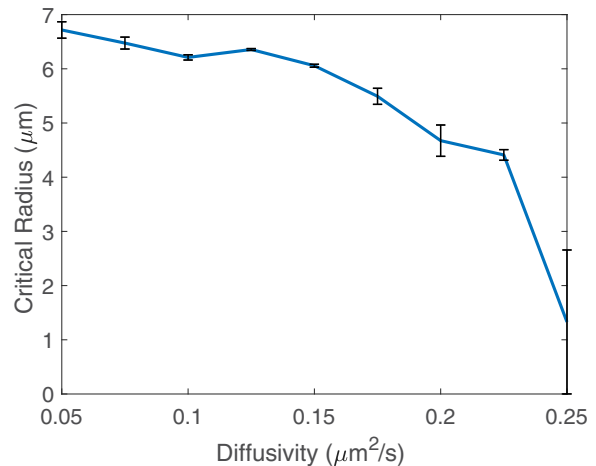


FIG. 16. Critical radius for propagation of  $K^+$  wavefronts as a function of the diffusion coefficients of the  $K^+$  ions ( $D_c$ , the diffusivity) from ABM simulations. An average of three runs is shown. The critical radii decrease as the  $K^+$  diffusivity increases. The error bars are the standard error mean of the three runs.

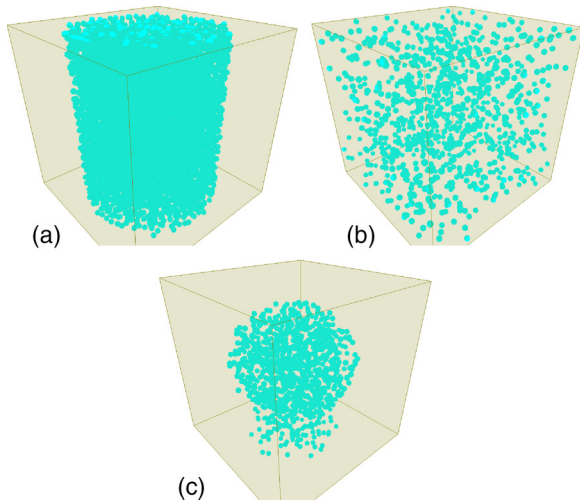


FIG. 17. Different bacterial biofilm geometries that were used for the FDF ABM in addition to a spherical geometry (Fig. 2): (a) a cylinder, (b) a cube, and (c) a mushroom shape.

sive behavior for the  $K^+$  wavefront dynamics was observed regardless of the rise and dormancy times. The curve shifts to later starting times with a higher dormancy time as expected.

#### IV. DISCUSSION

The parameters used in the 3D ABM FDF model for *E. coli* were initially inspired by the simulations of Blee *et al.* [16] for *B. subtilis*. These parameters were then adapted based on more specific information from *E. coli* [6].

In Fig. 4 power-law scaling occurs for the average  $K^+$  wavefront velocity on the diffusivity of the  $K^+$  ions. In Fig. 5

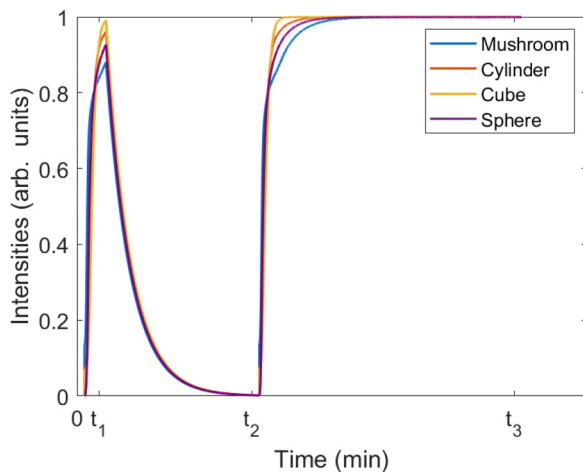


FIG. 18. Total intensity of the potassium ions averaged over an entire biofilm as a function of time for different biofilm shapes spiked at their centers. The parameters were kept constant throughout the different geometries: the  $K^+$  ion diffusivity ( $D_c$ ) was  $0.1 \mu\text{m}^2/\text{s}$ , the total potassium ions added ( $\sigma$ ) was  $5 \times 10^9$ , the firing threshold ( $c^*$ ) was  $1 \times 10^7$ , and the decay rate ( $k_s$ ) was  $5 \times 10^{-3}$ . The first wavefront of the FDF stopped at  $t_1 = 180$  s, and the second wavefront began (new hyperpolarization event) at  $t_2 = 1440$  s. The simulation stopped at  $t_3 = 3600$  s.

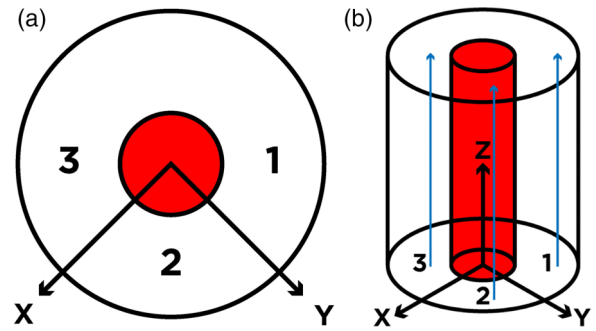


FIG. 19. Schematic diagram of a cylindrical biofilm with a cylindrical defect shown in red used in the simulation. The bacteria are randomly placed in the cylinder except for the area shown in red. (a) Top view of the plane perpendicular to the  $y$  axis. (b) Side view of the plane parallel to the  $y$  axis. The blue arrows indicate the directions in which the wavefront propagation was quantified.

there is also a clear power-law scaling for the instantaneous wavefront velocity on different  $K^+$  diffusivities, and the velocity is larger for larger radii. This unpredicted effect could be associated with the diversity found in microclusters within bacterial biofilms. Furthermore, the power-law exponents for the scaling of the instantaneous velocity are shown in Fig. 6, which depend on the radii. They fall in the expected range, 0.5–1, for a FDF model [7].

In Fig. 7 both simulation and experiment agree that the first peak is sharp and that the second wave plateaus. However, in the simulation, although the first peak is similar to experiments, there is a discrepancy between the rate at which the intensity increases (i.e., during hyperpolarization of the cells) for the second rise. More detailed models of ion channel kinetics are needed to describe this, e.g., Hodgkin-Huxley models for ion channel opening and models for cell to cell variability need to be considered [7,8]. The centrifugal  $K^+$  wavefront has a superdiffusive scaling exponent of  $\gamma$  of 1.21 for  $R^2$  on time (Fig. 8). For the centripetal  $K^+$  wavefront (Fig. 8) has a scaling exponent,  $\gamma$ , of 2.26, making it superballistic. Thus the nature of the dynamics changes as the wavefront collapses back into the biofilm.

The  $K^+$  wavefront velocity as a function of time for centrifugal waves is seen in Fig. 9(a), where there is an inverse proportionality. Figure 9(b) shows in contrast that the velocity of centripetal waves increases with time. As the  $K^+$  wavefront is propagating towards the center, the velocity increases monotonically. In Fig. 10(a) the  $K^+$  centrifugal wavefront velocity varies below a threshold curvature value, also suggesting a critical value for the radius. Figure 10(b) shows for the centripetal  $K^+$  wavefronts the velocity increases and then saturates at high curvature, which suggests that the larger curvatures contribute to the greater velocities. Both varieties of wavefront exhibit the plateau expected from the Eikonal approximation over a range of higher curvatures [7].

The  $K^+$  wavefront positions experience anomalous diffusion in the experimental data and are in agreement

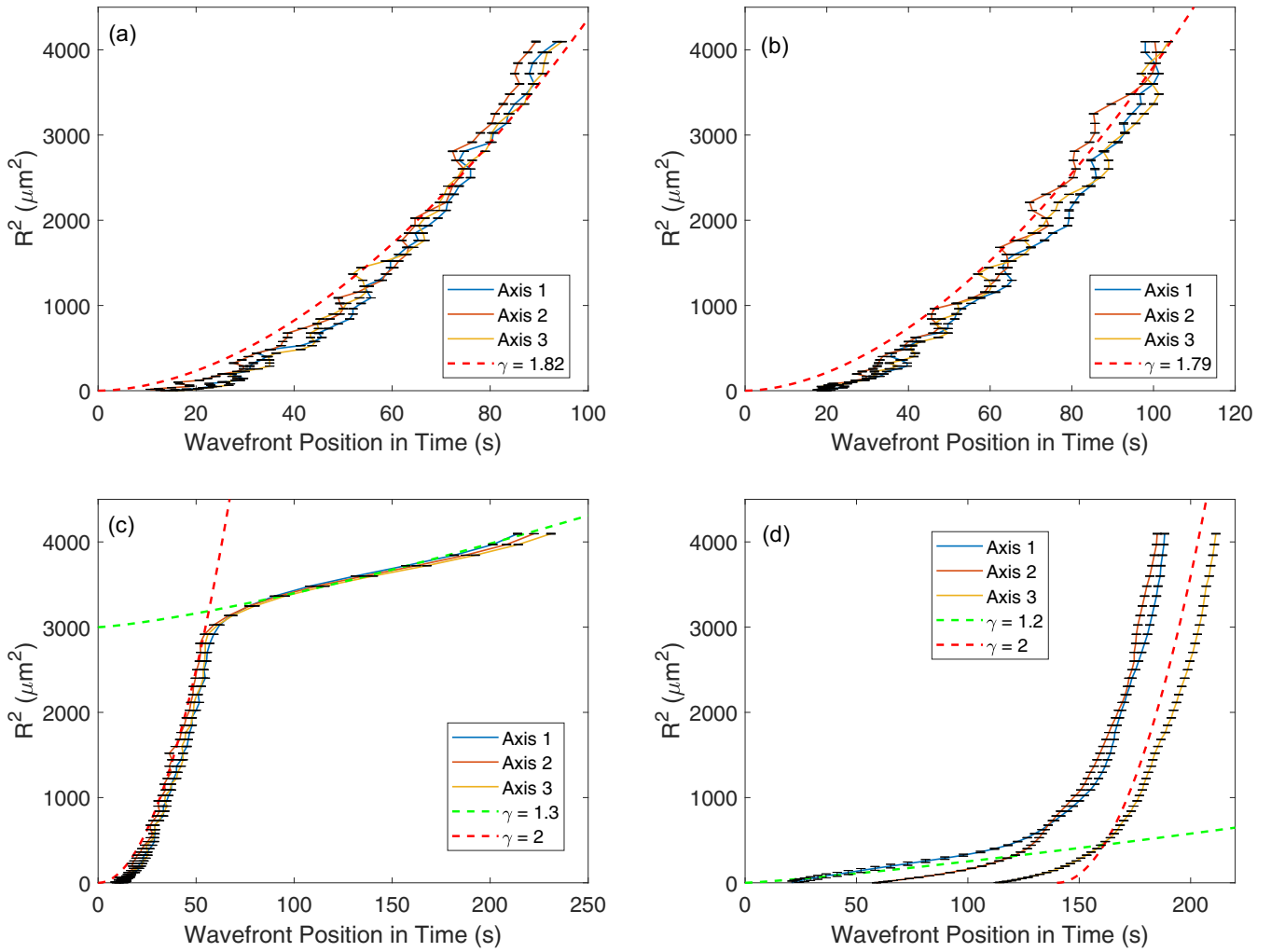


FIG. 20. Mean-square displacement,  $R^2$ , of the  $K^+$  wavefront as a function of time for (a) a cylinder, (b) a cube, (c) a mushroom-like shape, and (d) a cylinder with a cylindrical defect. The simulation parameters were kept constant for the different geometries. The  $K^+$  diffusivity ( $D_c$ ) was  $0.1 \mu\text{m}^2/\text{s}$ , the total  $K^+$  added ( $\sigma$ ) was  $5 \times 10^9$ , the firing threshold ( $c^*$ ) was  $1 \times 10^7$ , and the decay rate ( $k_s$ ) was  $5 \times 10^{-3}$ . The trend lines for different  $\gamma$  values are shown for the different regimes. The error bars are the standard mean error on the wavefronts for three runs.

with the simulation. The centripetal wave is superballistic, and the centrifugal wave is subballistic and superdiffusive. Furthermore, there is a slow decrease of the velocity for the centrifugal wavefront as a function of time in experiments [6], which looks similar to the model predictions in Fig. 9(a). However, the centripetal velocity wavefront in Fig. 9(b) is not in exact agreement with experiment. This suggests there is another mechanism unaccounted for in the model that limits its accuracy, such as heterogeneity of microclusters within the bacterial biofilms. It is suggested that *E. coli* biofilms have subpopulations of the cells with distinct phenotypes [3].

The scaling of the mean-square wavefront position ( $R^2$ ) with the power-law scaling factor  $\gamma$  on time for different  $K^+$  diffusion coefficients (Fig. 14) seems reasonable since the wavefront struggles to propagate for lower diffusion coefficients for the potassium ions and a more ballistic diffusion of the wavefront occurs.

In Fig. 15 higher values of the firing threshold ( $c^*$ ) for  $K^+$  ion release makes the  $K^+$  wavefront behave more subdiffusively as a function of time. The  $K^+$  wavefront lingers more

on each bacterium for high threshold values and therefore propagates slower.

Figure 16 shows decreasing the diffusion coefficient of the  $K^+$  ions causes the critical radius of the propagating wavefronts to decrease. Above the maximum value of  $K^+$  diffusivity shown in the figure, the critical radius ceased to exist. Furthermore, at higher firing thresholds ( $c^*$ ), there is a decrease of the critical radius.

The different biofilm geometries (sphere, cylinder, cube, and mushroom) cause only a minor changes to the dynamics of the globally averaged potassium ion concentration and show the double hyperpolarization phenomenon observed in experiments, Fig. 18. The  $R^2$  values as a function of time in Fig. 20 show that for the cylinder and the cube, the system has similar superdiffusive dynamics to the spherical biofilm. However, for the mushroom shape, the curve has a second regime where the superdiffusive behavior changes to a diffusive or subdiffusive-like behavior at short timescales. The beginnings of the three curves of the  $R^2$  as a function of time for the cylinder with a defect [Fig. 20(d)] all start as expected with axis 1 going first (it is closest to the point of

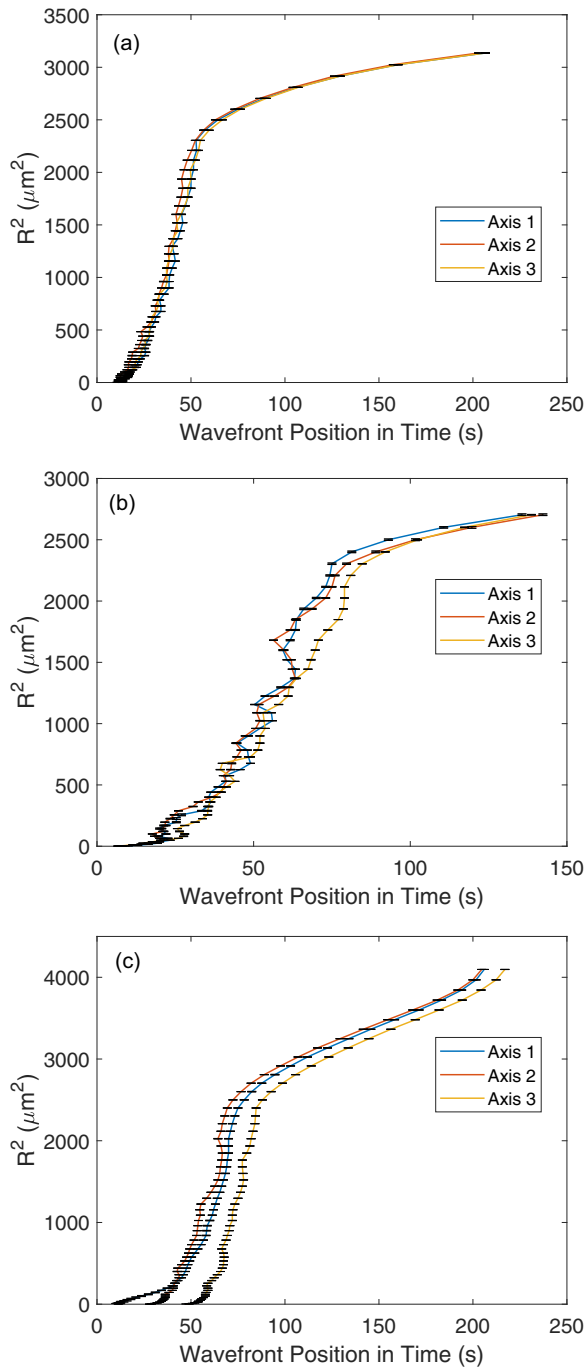


FIG. 21. Mean-square displacement,  $R^2$ , of the  $K^+$  wavefront as a function of time for (a) a small cylinder, (b) a small cube, and (c) a small cylinder with a cylindrical defect. The simulation parameters were kept constant for the different geometries. The  $K^+$  diffusivity ( $D_c$ ) was  $0.1 \mu\text{m}^2/\text{s}$ , the total  $K^+$  added ( $\sigma$ ) was  $5 \times 10^9$ , the firing threshold ( $c^*$ ) was  $1 \times 10^7$ , and the decay rate ( $k_s$ ) was  $5 \times 10^{-3}$ . The error bars are the standard mean error on the wavefronts for three runs.

stimulation), and axis 2 starting after a delay time and axis 3 starting after a longer delay. The behavior quickly changes from a subdiffusive to a superdiffusive behavior, suggesting that the waves propagate differently once the whole geometry along the axis is activated.

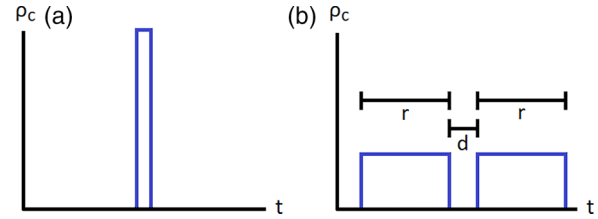


FIG. 22. Concentration profile of potassium ions released from a single bacterium as a function of time ( $t$ ).  $\rho_c$  is the potassium concentration density, i.e., the  $K^+$  concentration per unit time. The area of the rectangles equals the total  $K^+$  concentration released. (a) The initial FDF model with instantaneous release and a finite time step. (b) A sustained release time ( $r$ ) and a dormancy time ( $d$ ) are shown.

Interestingly, if the biofilm geometries are made smaller, a subdiffusive characteristic appears in all the geometries, similar to the mushroom-like shape. This suggests that the superdiffusive transport of  $K^+$  wavefronts at long times combines with the subdiffusive behavior at short times in biofilm geometries that have lower dimensionalities.

When introducing release and dormancy times for the firing of the potassium ions, the  $K^+$  wavefronts are not very different in terms of the superdiffusion of the wavefront position squared ( $R^2$ ) as a function of time. However, the  $K^+$  wavefront starts with different delay times (Fig. 23). This suggests that the transport of the  $K^+$  wavefront does not depend on the release and delay times and will be relatively robust to the opening and closing rates of the ion channels. Furthermore, the intensity profile is rescaled in amplitude by the release and dormancy times without changes to the shape. This suggests that the release and dormancy times influence only the maximum  $K^+$  wavefront amplitude, and the process is robust to minor variations in these parameters.

Anomalous diffusion of wavefronts in reaction-diffusion systems has not been studied extensively in the literature from

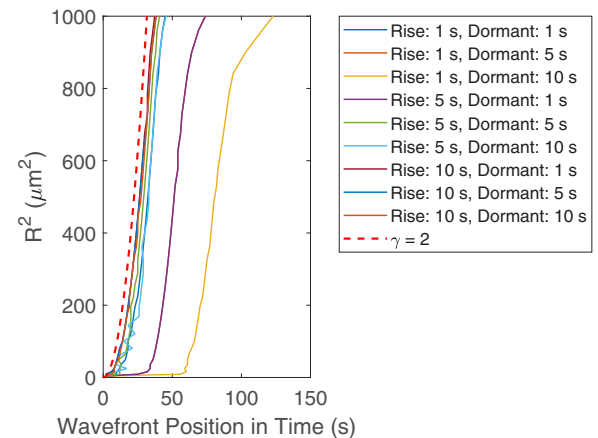


FIG. 23. Mean-square position ( $R^2$ ) of the  $K^+$  wavefront,  $R^2$ , as a function of time for different rise and dormancy times from ABM simulations. The  $K^+$  diffusivity ( $D_c$ ) was  $0.1 \mu\text{m}^2/\text{s}$ , the total  $K^+$  added ( $\sigma$ ) was  $5 \times 10^9$ , the firing threshold ( $c^*$ ) was  $1 \times 10^7$ , and the decay rate ( $k_s$ ) was  $5 \times 10^{-3}$ . The trend line is a power law with exponent  $\gamma = 2$  (dashed line) showing ballistic scaling.

the perspective of simulations [16] or experiments [6]. Analytic solutions to classical reaction-diffusion equations tend to predict diffusive ( $R^2 \sim t$ ) or ballistic ( $R^2 \sim t^2$ ) scaling of wavefront transport, but it is an inconvenient truth that the majority of real systems probably have intermediate scaling of wavefront position with time [29]. For the anomalous motion of single particles, standard models invoke non-Markovian effects (e.g., continuous time random walks or fractional Brownian motion) [29]. No non-Markovian effects were explicitly included in our simulations (classical diffusion was modeled for the ions, and ion release from bacteria is assumed fast on the timescale of the simulations; e.g., there are no fat tails in the probability distributions for ion release), so the physical origin of the anomalous wavefront dynamics is currently unclear and requires further research. At long timescales ( $t \rightarrow \infty$ ) and long distances from a biofilm ( $R \rightarrow \infty$ ) the concentration profile of  $K^+$  ions must resemble diffusion from a point source, so diffusive kinetics of ion transport are expected in the limiting regimes of long time and long distance scales. Furthermore, wavefront dynamics will terminate once all the bacteria have released their potassium, e.g., at the edge of the biofilm for centripetal wavefronts. Thus the anomalous kinetics of wavefronts will occur only over an intermediate range of timescales, but this is expected to be biologically relevant and corresponds to an experimentally accessible time window [6,16].

It would be interesting to segment confocal microscopy images of a real biofilm and then predict the wave fronts on real biofilm communities based on the FDF ABM. Percolation transitions for the propagation of electrical wavefronts are possible in mixed species biofilm, where one species is more susceptible to hyperpolarization. Different types of electrical signal quenching are also possible analogous to the phenomenon of *quorum quenching* which is observed biologically [34] and could be explored with ABM.

The model could also be further developed by adding different species in the model. That is, having agents with different characteristics, such as the threshold for firing and spatial positions, could provide a more realistic interpretation of common biofilms which contain many species of bacteria [3].

It is possible that the electrical response of many bacterial cells is anisotropic; e.g., gap junctions have been discovered in marine bacteria [35]. It would be interesting to model the

effect of electrical anisotropy (e.g., to place more ion channels on the axis of elongated cells) on the propagation of  $K^+$  wavefronts.

Future simulations can be developed that include the full Hodgkin-Huxley equations for the neuronal-like activity of the bacteria [7]. The current fire-diffuse-fire model provides a minimal model to describe a series of phenomena in light-stressed *E. coli* biofilms, e.g., the anomalous transport of wavefronts and the critical radius for wavefront propagation. However, additional experiments using electrical stimulation of *E. coli* biofilms demonstrate some nonlinear aspects of the hyperpolarization phenomena that will require a nonlinear Hodgkin-Huxley model for their explanation, e.g., hysteresis in  $K^+$  release. Electrical impedance spectroscopy measurements with *E. coli* biofilms also are providing additional information on the activity of ion channels that need to be included in agent-based models, e.g., neuromorphic negative capacitances due to  $K^+$  ion channels [36,37].

## V. CONCLUSIONS

Fire-diffuse-fire agent-based modeling provides a satisfactory description of many of the emergent phenomena observed in the electrical signaling of bacterial biofilms, e.g., when *E. coli* biofilms experience stress to blue light. Anomalous dynamics of the wavefronts are well described with a relatively simple fire-diffuse-fire mechanism calculated numerically with agent-based modeling. A critical radius for  $K^+$  wavefront propagation is an emergent property of the simulations and is observed in experiments. The dependence of  $K^+$  wavefront propagation on the biofilm geometry and defects in the biofilms was investigated, and it could motivate future experiments, e.g., to observe geometry dependent transitions between superdiffusive and subdiffusive scaling of the  $K^+$  wavefronts.

## ACKNOWLEDGMENTS

We thank Johanna Blee, Elyece Malnati, Kiera Moreno, Emily Gillot, and Harry Lipscomb for their contributions, as well as Jose Carlos Breña for his help with image design. Further, we thank Ovidio Cesar and Thiago Militino for their assistance with Java coding.

- 
- [1] K. J. Locey and J. T. Lennon, Scaling laws predict global microbial diversity, *Proc. Nat. Acad. Sci. USA* **113**, 5970 (2016).
  - [2] T. A. Waigh, *The Physics of Bacteria: From Cells to Biofilms* (Cambridge University Press, Cambridge, 2024).
  - [3] H.-C. Flemming, J. Wingender, U. Szewzyk, P. Steinberg, S. A. Rice, and S. Kjelleberg, Biofilms: An emergent form of bacterial life, *Nat. Rev. Microbiol.* **14**, 563 (2016).
  - [4] M. B. Miller and B. L. Bassler, Quorum sensing in bacteria, *Annu. Rev. Microbiol.* **55**, 165 (2001).
  - [5] I. Olsen, Biofilm-specific antibiotic tolerance and resistance, *Eur. J. Clin. Microbiol. Infect. Dis.* **34**, 877 (2015).
  - [6] E. Akabuogu, V. Carneiro Da Cunha Martorelli, R. Krašovec, I. Roberts, and T. Waigh, Emergence of ion-channel mediated electrical oscillations in *Escherichia coli* biofilms., eLife (to be published).
  - [7] J. Keener and J. Sneyd, *Mathematical Physiology* (Springer New York, New York, 2009).
  - [8] W. Gerstner, W. M. Kistler, R. Naud, and L. Paninski, *Neuronal Dynamics: From Single Neurons to Networks and Models of Cognition* (Cambridge University Press, Cambridge, 2014).
  - [9] A. Prindle, J. Liu, M. Asally, S. Ly, J. Garcia-Ojalvo, and G. M. Sueel, Ion channels enable electrical communication in bacterial communities, *Nature (London)* **527**, 59 (2015).

- [10] M. Hennes, N. Bender, T. Cronenberg, A. Welker, and B. Maier, Collective polarization dynamics in bacterial colonies signify the occurrence of distinct subpopulations, *PLoS Biol.* **21**, e3001960 (2023).
- [11] J. Blee, I. Roberts, and T. Waigh, Membrane potentials, oxidative stress and the dispersal response of bacterial biofilms to 405 nm light, *Phys. Biol.* **17**, 036001 (2020).
- [12] C. Mounfield, *The Handbook of Agent Based Modelling* (Independent Publishing, 2020).
- [13] R. Yu, H. Zhang, and B. Guo, Conductive biomaterials as bioactive wound dressing for wound healing and skin tissue engineering, *Nano-Micro Lett.* **14**, 1 (2022).
- [14] H. J. Jensen, *Complexity Science: The Study of Emergence* (Cambridge University Press, Cambridge, 2022).
- [15] E. Bonabeau, Agent-based modeling: Methods and techniques for simulating human systems, *Proc. Natl. Acad. Sci. USA* **99**, 7280 (2002).
- [16] J. A. Blee, I. S. Roberts, and T. A. Waigh, Spatial propagation of electrical signals in circular biofilms: A combined experimental and agent-based fire-diffuse-fire study, *Phys. Rev. E* **100**, 052401 (2019).
- [17] J. Humphries, L. Xiong, J. Liu, A. Prindle, F. Yuan, H. A. Arjes, L. Tsimring, and G. M. Suel, Species-independent attraction to biofilms through electrical signaling, *Cell* **168**, 200 (2017).
- [18] L. M. Rooney, W. B. Amos, P. A. Hoskisson, and G. McConnell, Intra-colony channels in *E. coli* function as a nutrient uptake system, *ISME J.* **14**, 2461 (2020).
- [19] R. Metzler and J. Klafter, The restaurant at the end of the random walk: Recent developments in the description of anomalous transport by fractional dynamics, *J. Phys. A: Math. Gen.* **37**, R161 (2004).
- [20] W. H. Vicenç Méndez and S. Fedotov, *Reaction-Transport Systems: Mesoscopic Foundations, Fronts, and Spatial Instabilities* (Springer, Berlin, 2010).
- [21] T. E. Goroehowski, A. Matyjaszkiewicz, T. Todd, N. Oak, K. Kowalska, S. Reid, K. T. Tsaneva-Atanasova, N. J. Savery, C. S. Grierson, and M. di Bernardo, Bsim: An agent-based tool for modeling bacterial populations in systems and synthetic biology, *PLoS ONE* **7**, e42790 (2012).
- [22] See Supplemental Material at <http://link.aps.org/supplemental/10.1103/PhysRevE.109.054402> for the general parameters used and a comparison to a previous 2D model as well as videos for the different geometries being stimulated at the bottom (a mushroom, a cylinder, and a cube) and at the center (a sphere). These stimulations produced the total intensity graphs shown in Fig. 18. A brief description of the videos is also given, which includes Ref. [23].
- [23] B. R. Martin and G. Shaw, *Mathematics for Physicists* (John Wiley Sons, 2015).
- [24] W. N. Reynolds, J. E. Pearson, and S. P.-Dawson, Dynamics of self-replicating patterns in reaction diffusion systems, *Phys. Rev. Lett.* **72**, 2797 (1994).
- [25] G. D. Smith, J. E. Keizer, M. D. Stern, W. J. Lederer, and H. Cheng, A simple numerical model of calcium spark formation and detection in cardiac myocytes, *Biophys. J.* **75**, 15 (1998).
- [26] S. Coombes, The effect of ion pumps on the speed of travelling waves in the fire-diffuse-fire model of  $\text{Ca}^{2+}$  release, *Bull. Math. Biol.* **63**, 1 (2001).
- [27] E. Niggli,  $\text{Ca}^{2+}$  on the move: What is better—fire and forget, or fire—diffuse—fire? *J. Physiol.* **588**, 1391 (2010).
- [28] P. B. Dieterle and A. Amir, Diffusive wave dynamics beyond the continuum limit, *Phys. Rev. E* **104**, 014406 (2021).
- [29] N. Korabel and T. A. Waigh, Heterogeneous anomalous transport in cellular and molecular biology, *Rep. Prog. Phys.* **86**, 126601 (2023).
- [30] R. Metzler, J.-H. Jeon, A. G. Cherstvy, and E. Barkai, Anomalous diffusion models and their properties: non-stationarity, non-ergodicity, and ageing at the centenary of single particle tracking, *Phys. Chem. Chem. Phys.* **16**, 24128 (2014).
- [31] S. B. Alves, G. F. de Oliveira, Jr., L. C. de Oliveira, T. P. de Silans, M. Chevrollier, M. Oria, and H. L. D. de S. Cavalcante, Characterization of diffusion processes: Normal and anomalous regimes, *Physica A: Stat. Mech. Appl.* **447**, 392 (2016).
- [32] P. Balbuena, K. Johnston, P. Rossky, and J. Hyun, Aqueous ion transport properties and water reorientation dynamics from ambient to supercritical conditions, *J. Phys. Chem. B* **102**, 3806 (1998).
- [33] M. Toyofuku, T. Inaba, T. Kiyokawa, N. Obana, Y. Yawata, and N. Nomura, Environmental factors that shape biofilm formation, *Biosci. Biotech. Biochem.* **80**, 7 (2016).
- [34] S. Fetzner, Quorum quenching enzymes, *J. Biotech.* **201**, 2 (2015).
- [35] G. L. Weiss, A.-K. Kieninger, I. Maldener, K. Forchhammer, and M. Pilhofer, Structure and function of a bacterial gap junction analog, *Cell* **178**, 374 (2019).
- [36] A. Bou and J. Bisquert, Impedance spectroscopy dynamics of biological neural elements: From memristors to neurons and synapses, *J. Phys. Chem. B* **125**, 9934 (2021).
- [37] K. S. Cole, *Membranes, Ions and Impulses: A Chapter of Classical Biophysics* (University of California Press, California, 1968).